Forthcoming Articles have been peer-reviewed and accepted for publication in *InterPore Journal*. To make research available as early as possible, accepted manuscripts may be published online prior to completion of the final production process. These versions have not yet undergone final formatting, proofreading, or author corrections and therefore do not represent the **Version of Record**. Minor changes may occur during the final production process. The article will be updated with the final Version of Record when it is published in its assigned journal issue. **Forthcoming Articles should be cited using their DOI, which will remain the same after publication of the final Version of Record.**

Please cite the following article as:

Riess, A.,Hasanzade, R., Tchelepi, H., & Jenny, P. (2026). Coupled Hyperbolic Subsurface Flow (CHSF)Model to Solve Buoyant Two-Phase Flow and Transport in Heterogeneous Porous Media. InterPore Journal. Forthcoming Article.
https://doi.org/10.69631/4mz6cd49

Received on: 30 Nov. 2025
Accepted on: 12 Aug. 2026
Published online (Accepted version): 23 Aug. 2026

Coupled Hyperbolic Subsurface Flow (CHSF) Model to Solve Buoyant Two-Phase Flow and Transport in Heterogeneous Porous Media

Keywords Porous media, multiphase flow, subsurface flow and transport, hyperbolic conservation laws, Riemann solver

Abstract

Traditional methods for simulating buoyant two-phase flow and transport in porous media involve solving large systems of tightly coupled discrete equations, which involves non-local operations. In [16], a new approach was proposed which requires no global system to be solved and thus only relies on local computations. This makes it well-suited for large-scale parallel processing on multiple CPUs and GPUs. The new coupled hyperbolic subsurface flow (CHSF) model for two phase flow and transport, was compared to the Implicit Method and an established general purpose reservoir simulator (GPRS), showing that it is highly efficient and accurate for homogeneous media. However, numerical artifacts appear if it is employed for heterogeneous media. In this work, these artifacts are addressed, and to resolve the deficiencies, a novel multi-dimensional Rankine-Hugoniot-Riemann (MD-RHR) solver is devised. Numerical experiments demonstrate that with this MD-RHR solver the CHSF model can deal with heterogeneous permeability fields and accurately reproduces reference results.

1 Introduction

Subsurface reservoirs are geological formations that can contain a range of fluids, such as water, hydrocarbons, or CO_2 in often complex porous structures. For example, depleted hydrocarbon reservoirs and saline aquifers can be used as large-scale underground storage sites for hydrogen [14]. Another example is related to capturing carbon from emission sources and storing it in subsurface reservoirs, which is a promising technology for reducing

CO_2 emissions into the atmosphere [9].

Observing and measuring subsurface flow is usually very difficult. Therefore, numerical simulation is an essential tool to predict the behavior of fluid phases in reservoirs [20]. Flow and transport of two immiscible fluid phases in porous media are governed by Darcy's law, the continuity equation and a saturation transport equation. Conventional methods, such as the Fully Implicit or the IMPES (Implicit Pressure, Explicit Saturation) methods, directly attempt to solve this system, which entails an elliptic or parabolic flow equation for the pressure that has to be solved globally, leading to large systems of tightly coupled linear equations that are computationally expensive to solve [3].

Recently, a completely novel method, here called coupled hyperbolic subsurface flow (CHSF) model [16], was proposed that bypasses this expensive global system. The governing equations are cast in a hyperbolic system that can be solved using only local computations. The foundation of this system consists of the isothermal Euler equations, with a source term derived from Darcy's law accounting for the resistance due to the porous material. Since it only requires local computations one can expect that it is well-suited for massive parallelization and computations on multiple CPUs and GPUs.

In this paper, this hyperbolic system is analyzed further. Its analytical solution for a simplified problem is compared to the solution of the classical system based on Darcy's law, and error estimates are given.

As described in [16], in the CHSF method the system is solved efficiently and accurately with a finite volume method relying on a characteristics-based Riemann solver. In the tests with homogeneous permeability the solutions of the new hyperbolic method compare very well with those obtained with the Implicit Method and GPRS [1].

However, for heterogeneous permeability fields, such as those with nearly impermeable shales, CHSF incorrectly allows penetration of fluid into the low permeability regions. This happens because the Riemann solver does not take the large source terms into account, leading to inaccurate numerical fluxes. In this paper we devise a novel multi-dimensional Rankine-Hugoniot-Riemann (MD-RHR) solver and demonstrate that it can resolve this issue.

The remainder of this paper is organized as follows: In Section 2 we introduce the governing equations of CHSF, Section 3 outlines the details of the MD-RHR solver. Section 4 presents the numerical experiments and in Section 5, we draw conclusions and future work.

2 Governing Equations

The description of the hyperbolic system given here is based on the more detailed derivation in [16]. The aspects relevant for this paper are highlighted here again for completeness.

We start with the classical equations for buoyant two-phase flow and transport in porous media. Our goal is to construct a hyperbolic system of equations that can be solved at low cost only using local operations and that well approximates the classical description. In the derivation of this system, two algorithmic parameters are introduced, and three approximations are made. Accuracy and computational cost of the method depend on the choice of these two parameters. This relationship is also examined in this section.

2.1 Classical System

We start with the classical system for incompressible buoyant two-phase flow using Darcy's law with a gravity term, with

$$\mathbf{u} = -\lambda k \nabla p + k\gamma \mathbf{g} \quad \text{and} \quad \nabla \cdot \mathbf{u} = 0, \tag{1}$$

where $\mathbf{u}$ is the total Darcy velocity, p the pressure, k the permeability, and $\mathbf{g}$ the gravitational acceleration. Further,

$$\lambda = \underbrace{\frac{k_{r1}}{\mu_1}}_{\lambda_1} + \underbrace{\frac{k_{r2}}{\mu_2}}_{\lambda_1} \quad \text{and} \quad \gamma = \lambda_1 \rho_1 + \lambda_2 \rho_2 \tag{2}$$

with relative permeability k_{ri}, dynamic viscosity μ_i, and phase density ρ_i of phase i.

The relative permeabilities are functions of the phase saturations S_i; here only two phases are considered and the notation $S = S_1 = 1 - S_2$ with the quadratic relationships [10]

$$k_{r1}(S) = S^2 \quad \text{and} \quad k_{r2}(S) = (1 - S)^2 \tag{3}$$

are used throughout the paper (for simplicity, but without loss of generality). Eq. (1) is coupled with the transport equation [5]

$$\frac{\partial \phi S}{\partial t} + \nabla \cdot \mathbf{u}_1 = 0. \tag{4}$$

To obtain the velocity $\mathbf{u}_1$ of phase 1, the fractional flow relationship

$$\mathbf{u}_1 = \underbrace{\frac{\lambda_1}{\lambda}}_{f_1}\,\mathbf{u} + \underbrace{\frac{\lambda_1\lambda_2}{\lambda}(\rho_1-\rho_2)k}_{f_{12}}\,\mathbf{g} \tag{5}$$

is used; its derivation is given in the Appendix A.1. The functions f_1 and f_{12} are used for convenience.

Most conventional numerical methods for incompressible buoyant two-phase flow and transport in porous media solve equations (1) and (4) directly. On the other hand, our new approach uses a completely different system of governing equations which is shown in the following.

2.2 Hyperbolic System

The derivation of the hyperbolic system is explained here for 2D problems, but the extension to 3D is straightforward. We start with the isothermal Euler equations

$$\frac{\partial}{\partial t}\begin{pmatrix}\rho\\ \rho u\\ \rho v\end{pmatrix} + \frac{\partial}{\partial x}\begin{pmatrix}\rho u\\ \rho u^2+p\\ \rho uv\end{pmatrix} + \frac{\partial}{\partial y}\begin{pmatrix}\rho v\\ \rho uv\\ \rho v^2+p\end{pmatrix} = \begin{pmatrix}0\\0\\0\end{pmatrix} \tag{6}$$

with the state equation

$$p = \rho c^2. \tag{7}$$

In Eq. (6) we have the velocity $\mathbf{u} = (u,v)^{\mathrm{T}}$, the density ρ, and the pressure p. It is important to note that ρ is a purely algorithmic variable that carries no physical meaning and has nothing to do with the physical phase densities. Instead, it is related to the parameter ρ_{ref} of this method, which we call the reference density. Similarly, the constant c that takes the place of the speed of sound in the state equation (7) is also a parameter without physical meaning.

One should choose the parameters c and ρ_{ref} with care as they determine the approximation power of the system (6) and the computational cost of the method, which is shown later in subsection 2.3.

The Euler equations originate from gas dynamics, and by themselves they are unrelated to flow in porous media. They are used here as they are hyperbolic and because they lead to nearly incompressible solutions if the Mach number $\mathrm{Ma} = |\mathbf{u}|/c$ remains small enough (less than approximately 0.3) [2]. Keeping the compressibility weak is our first approximation.

Further, system (6) only leads to nearly divergence free velocity fields, if the relative

density variations are kept small along any streamline, as shown in [16]. This is the case if the density stays relatively close to the reference density ρ_{ref} everywhere, which is our second approximation.

To find equations that describe flow in porous media, Darcy's law has to be accounted for. Therefore we add the source terms (8)

$$Q_x = -\frac{1}{\lambda k}u + \frac{\gamma}{\lambda}g_x \quad \text{and} \quad Q_y = -\frac{1}{\lambda k}v + \frac{\gamma}{\lambda}g_y \tag{8}$$

to the right-hand sides of the second and third equations of system (6), which then can be rewritten as

$$\underbrace{\frac{\partial}{\partial t}\begin{pmatrix}\rho u\\ \rho v\end{pmatrix} + \frac{\partial}{\partial x}\begin{pmatrix}\rho u^2\\ \rho uv\end{pmatrix} + \frac{\partial}{\partial y}\begin{pmatrix}\rho uv\\ \rho v^2\end{pmatrix}}_{\mathbf{M}} + \nabla p = \underbrace{-\frac{1}{\lambda k}\mathbf{u} + \frac{\gamma}{\lambda}\mathbf{g}}_{\mathbf{Q}}. \tag{9}$$

If the terms $\mathbf{M}$ become negligible compared to $\mathbf{Q}$, then the momentum balance (9) simplifies to Darcy's law. This is our third approximation.

Here, the velocity in the Euler equations (6) is reinterpreted as the total Darcy velocity; in this paper the term "velocity" is used throughout. Note that $\mathbf{u}$ is not the fluid velocity at pore scale, but the volume averaged one at Darcy scale.

Moreover, the transport equation (4) with the fractional flow expression (5) for the phase velocity is included as a fourth equation. By defining $m_x = \rho u$, $m_y = \rho v$, and $s = \rho S\phi$ we arrive at the full system

$$\frac{\partial}{\partial t}\begin{pmatrix}\rho\\ m_x\\ m_y\\ s\end{pmatrix} + \frac{\partial}{\partial x}\begin{pmatrix}m_x\\ m_x^2/\rho + \rho c^2\\ m_x m_y/\rho\\ f_1 m_x + f_{12}\rho g_x\end{pmatrix} + \frac{\partial}{\partial y}\begin{pmatrix}m_y\\ m_x m_y/\rho\\ m_y^2/\rho + \rho c^2\\ f_1 m_y + f_{12}\rho g_y\end{pmatrix} = \begin{pmatrix}0\\ -m_x/(\rho\lambda k) + g_x\gamma/\lambda\\ -m_y/(\rho\lambda k) + g_y\gamma/\lambda\\ 0\end{pmatrix} \tag{10}$$

as defined in [16]. We refer to Eq. (10) as the CHSF model.

2.3 Choice of Parameters

To derive the full system, three approximations have been made, all of which introduce a modeling error. This modeling error means that solutions of Eq. (10) do not exactly satisfy the underlying physical laws (1) and (4). However, we can control the error by choosing c and ρ_{ref} and, at least in theory, make it arbitrarily small.

The three sources of modeling error can be linked to three dimensionless numbers that all have to remain small:

1. Mach number: The Euler equations only describe nearly incompressible flow if the Mach number $\mathrm{Ma}_{\max} = |\mathbf{u}|_{\max}/c$ remains small.

2. Relative density variations: To obtain a divergence free velocity, the largest density difference relative to the reference density, i.e., $\delta\hat{\rho}_{\max} = (\rho_{\max} - \rho_{\min})/\rho_{\mathrm{ref}}$, must remain small.

3. Source term dominance: In the second and third equations, the source term must dominate the inertial terms, which typically is the case if $\mathrm{R}_{\max} = (|\mathbf{u}|\rho k\lambda)_{\max}/L$ remains small, where

To analyze the errors introduced by considering the CHSF system instead of the classical equation, analytical solutions of a simple test case, i.e., of 1D steady state single-phase flow without gravity, are compared. The fluid is driven by setting a pressure p_{L} at the left side of the domain (at $x = 0$) and a velocity $u_{\mathrm{R}} > 0$ at the right side (at $x = L$). The derivations of both analytical solutions are presented in the Appendix A.2.

For the following, we choose

$$p_{\mathrm{L}} := \rho_{\mathrm{ref}} c^2. \tag{11}$$

Naturally, the choice of the parameters ρ_{ref} and c changes the boundary conditions. However, according to Darcy's law (1), the flow depends only on pressure differences, not the absolute value of the pressure. Thus, the choice of p_{L} does not change the flow behavior given by Darcy's law. This allows us to compare the CHSF system to Darcy's law for different choices of ρ_{ref} and c.

For this simple problem, we estimate how $\mathrm{Ma}_{\max}$, $\delta\hat{\rho}_{\max}$ and $\mathrm{R}_{\max}$ depend on c and ρ_{ref}:

$$\mathrm{Ma}_{\max} = \frac{u_{\mathrm{R}}}{c} \tag{12}$$

$$\delta\hat{\rho}_{\max} = 1 - \frac{u_{\mathrm{L}}}{u_{\mathrm{R}}} \leq \frac{\mu L}{k_{\min}} \frac{u_{\mathrm{R}}}{\rho_{\mathrm{ref}}(c^2 - u_{\mathrm{R}}^2)} \tag{13}$$

$$\mathrm{R}_{\max} = \frac{\rho_{\mathrm{ref}} u_{\mathrm{R}} k_{\max}}{\mu L} \tag{14}$$

A derivation for expression (13) is given in Appendix A.3.

Furthermore, we are interested in how the computational cost depends on the parameters. The time step size is limited through the CFL condition by the highest wave speed,

$$\Delta t = C_{\mathrm{CFL}} \frac{\Delta x}{|u|_{\max} + c} = C_{\mathrm{CFL}} \frac{\Delta x}{|u|_{\max}} \left(1 + \mathrm{Ma}_{\max}^{-1}\right)^{-1}, \tag{15}$$

where Δx denotes the (constant) grid spacing and C_{CFL} is the CFL number. This shows that for smaller $\mathrm{Ma}_{\max}$ more time steps are required. Generally, there is a trade-off

between computational cost and model accuracy. The lower the modeling error the smaller the time step needs to be.

For classical solvers of transport in porous media, the time step is limited by the largest flow speed, i.e.,

$$\Delta t_{\text{classical}} = C_{\text{CFL}} \frac{\Delta x}{|u|_{\max}}, \tag{16}$$

which shows that the timestep of the CHSF method is smaller by a factor $\left(1 + \text{Ma}_{\max}^{-1}\right)^{-1}$. Moreover, implicit methods allow for larger C_{CFL}, but this leads to lower accuracy.

Nevertheless, since in the CHSF method both flow and transport updates rely only on local calculations, for massive parallel computations it may be cheaper compared to conventional methods despite the smaller time step. The method is presented here as a proof of concept, and we did not investigate the computational cost further at this time.

Figure 1 compares analytical solutions of the CHSF equations for different choices of c and ρ_{ref} to the classical solution. The values of $\text{Ma}_{\max}$, $\delta\hat{\rho}_{\max}$ and $\text{R}_{\max}$ are given in Table 1. The parameters c and ρ_{ref} have been chosen such that the types of error that the three dimensionless numbers represent can easily be compared:

- along the rows $\text{Ma}_{\max}$ is constant,
- along the anti-diagonals $\delta\hat{\rho}_{\max}$ is similar, and
- along the columns $\text{R}_{\max}$ is of the same order of magnitude.

	$\rho_{\text{ref}} = 1$	$\rho_{\text{ref}} = 4$	$\rho_{\text{ref}} = 16$
$c = 1$	$\text{Ma}_{\max} = 0.5$ $\delta\hat{\rho}_{\max} = 0.6112567$ $\text{R}_{\max} = 0.0971858$	$\text{Ma}_{\max} = 0.5$ $\delta\hat{\rho}_{\max} = 0.2600232$ $\text{R}_{\max} = 0.7399768$	$\text{Ma}_{\max} = 0.5$ $\delta\hat{\rho}_{\max} = 0.0779063$ $\text{R}_{\max} = 3.6883748$
$c = 2$	$\text{Ma}_{\max} = 0.25$ $\delta\hat{\rho}_{\max} = 0.2286319$ $\text{R}_{\max} = 0.192842$	$\text{Ma}_{\max} = 0.25$ $\delta\hat{\rho}_{\max} = 0.0641789$ $\text{R}_{\max} = 0.9358211$	$\text{Ma}_{\max} = 0.25$ $\delta\hat{\rho}_{\max} = 0.0165097$ $\text{R}_{\max} = 3.9339611$
$c = 4$	$\text{Ma}_{\max} = 0.125$ $\delta\hat{\rho}_{\max} = 0.06142$ $\text{R}_{\max} = 0.234645$	$\text{Ma}_{\max} = 0.125$ $\delta\hat{\rho}_{\max} = 0.0157431$ $\text{R}_{\max} = 0.9842569$	$\text{Ma}_{\max} = 0.125$ $\delta\hat{\rho}_{\max} = 0.0039601$ $\text{R}_{\max} = 3.9841595$

Table 1: The values of $\text{Ma}_{\max}, \delta\hat{\rho}_{\max}, \text{R}_{\max}$ for different combinations of c and ρ_{ref}

According to Figure 1, the total error decreases as ρ_{ref} and c increase. For this simplified problem, the error represented by $R_{\max}$ is negligible. For more complex, i.e., heterogeneous and two-dimensional, this has to be taken into account, as shown in Appendix C.1. Note that this analysis does not show time-dependent or numerical errors. For example, for large values of c deviations caused by pressure waves may arise, as shown in [16].

The tests shown in Figure 1 demonstrate that the modeling error of the hyperbolic system

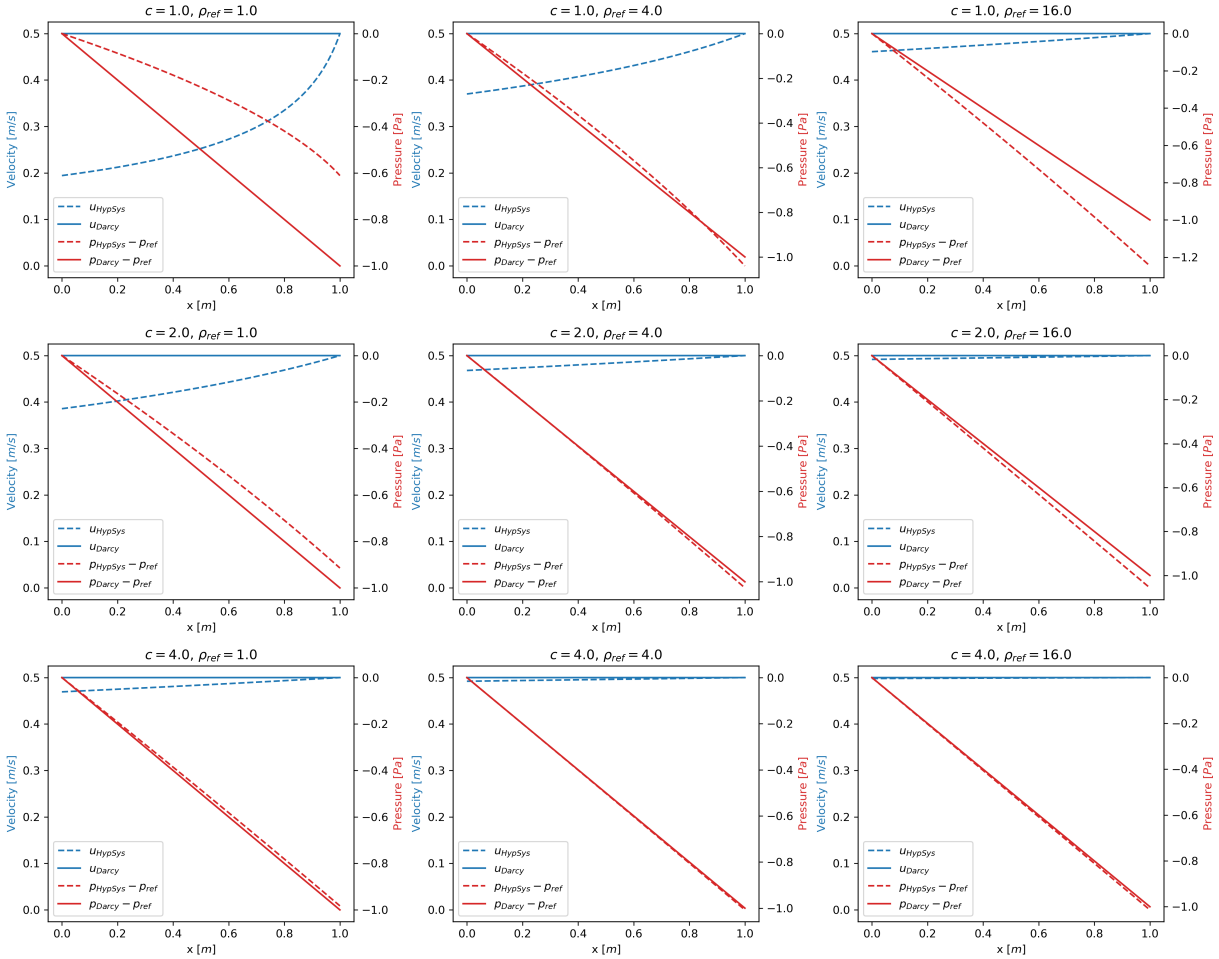


Figure 1: Incompressible, steady 1D test case: Comparison of analytical flow solutions obtained from the classical equations and the CHSF system for different values of c and ρ_{ref}. The pressure relative to the pressure p_{L} at the left boundary is shown.

strongly depends on the choice of the parameters. For more complex (not steady-state and two-dimensional) problems, finding the optimal parameters before running the computation can be difficult. One potential solution to this could be to adjust the parameters on the fly. Since it is known how the error scales with the parameters, it should be possible to tweak them if necessary as the simulation is running. However, this has not yet been tested.

3 Riemann Solver

As described in [16], the hyperbolic system (10) is solved with a finite volume method using an approximate Riemann solver. A Cartesian mesh is used for simplicity, and the

values in a cell with indexes i and j are updated as

$$\mathbf{U}_{n+1}^{i,j} = \mathbf{U}_{n}^{i,j} - \Delta t \left(\frac{1}{\Delta x} \left(\mathbf{F}_{x}^{i+1/2,j} - \mathbf{F}_{x}^{i-1/2,j} \right) + \frac{1}{\Delta y} \left(\mathbf{F}_{y}^{i,j+1/2} - \mathbf{F}_{y}^{i,j-1/2} \right) \right)_{n \to n+1} + \Delta t \mathbf{Q}_{n \to n+1}^{i,j}. \tag{17}$$

In Eq. (17) $\mathbf{F}_{x}^{i+1/2,j}$,$\mathbf{F}_{x}^{i-1/2,j}$,$\mathbf{F}_{y}^{i,j+1/2}$ and $\mathbf{F}_{y}^{i,j-1/2}$ are the fluxes at the right, left, top and bottom cell interfaces, Δt is the time step size, and Δx and Δy are the horizontal and vertical grid spacings, respectively. The cell average of $\mathbf{U}$ at the n^{th} time step is denoted as $\mathbf{U}_{n}^{i,j}$, and the cell average of the source term, $\mathbf{Q}_{n \to n+1}^{i,j}$, is treated implicitly for better stability. Note that the cell update is local as it depends only on the fluxes to the neighboring cells and the source term in the cell.

3.1 Ordinary Riemann Solver

The ordinary approximate Riemann solver employed in [16] relies on the method of characteristics and is based on solving one-dimensional Riemann problems at the cell interfaces, whereas the source terms are ignored. Thus, this ordinary Riemann solver finds the fluxes by solving

$$\frac{\partial}{\partial t}\mathbf{U} + \frac{\partial}{\partial x}\mathbf{F}_{x}(\mathbf{U}) = 0 \quad \text{and} \quad \frac{\partial}{\partial t}\mathbf{U} + \frac{\partial}{\partial y}\mathbf{F}_{y}(\mathbf{U}) = 0 \tag{18}$$

at the vertical and horizontal cell interfaces, respectively. Because the Riemann solver splits the system into simplified one-dimensional problems (18), it cannot produce an exact solution to the full system (10). Solving general multidimensional hyperbolic systems of conservation laws is very difficult, as discussed in [6] and [23], especially in higher dimensions, and we generally have to accept some numerical error. Despite not producing exact solutions, the Riemann solver is a well-established method for solving this type of problem.

In [16] it is shown how second order accuracy can be achieved through piecewise linear reconstruction of the cell values. It was demonstrated that this Riemann solver is very effective for natural convection problems with homogeneous permeability fields, i.e., the results produced by the hyperbolic method compare very well to those of a general purpose reservoir simulator.

However, when the CHSF method is used for cases with heterogeneous permeability fields, e.g. with nearly impermeable shales, the solutions exhibit unphysical artifacts. Such an example is shown in Figure 2.

The problem is that the large source term $\mathbf{Q}$ is not taken into account by the Riemann

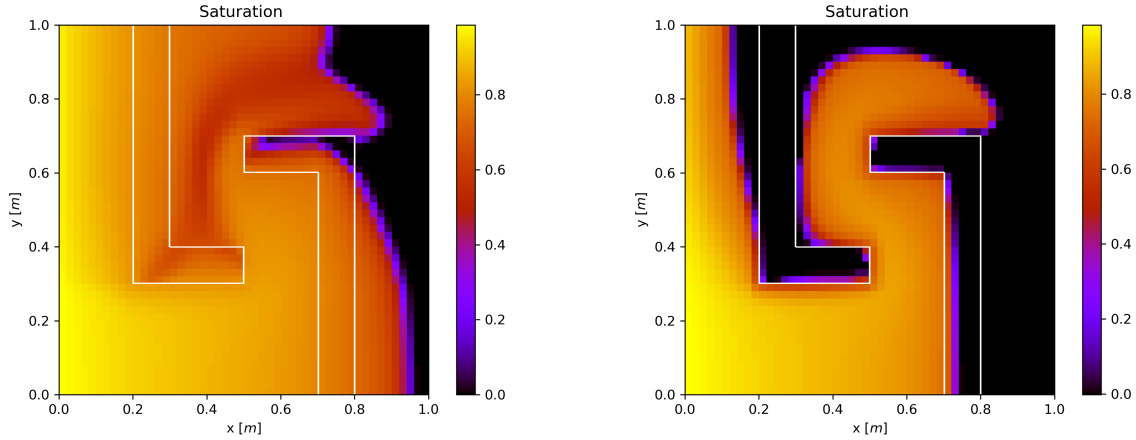


Figure 2: Two phase Flow and transport around nearly impermeable shales: The flow driven by a pressure difference of 1 Pa between left and right boundaries after 30 s. The top and bottom boundaries have no-flux boundary conditions. The nearly impermeable shales are marked by white lines. Initially, the domain is filled with the second phase, then the first phase enters through the left boundary. The CHSF method with first order spatial reconstruction (left) predicts severe and unphysical penetration of the second phase into the shales. With second order spatial reconstruction (right) this numerical artifact is reduced, but still present.

solver, since the characteristics and Riemann invariants were derived for the homogeneous systems (18). Therefore, the fluxes computed by the solver become inaccurate for large source terms.

3.2 Rankine-Hugoniot-Riemann Solver

Directly taking into account the source term by the Riemann solver would be tedious and very difficult. Instead, as shown next, it is possible to redistribute the source term within the cells ahead of the flux calculations to restore homogeneous conditions around the cell interfaces.

In principle, the source term is smoothly distributed across the whole domain, and for numerical calculations its integrals over individual cells are considered. Now, e.g. before solving Riemann problems at the vertical cell interfaces, these cell integrals are cast in a horizontal flux jump at the cell centers. Note that in order to be consistent, these flux jumps have to satisfy the Rankine-Hugoniot conditions, i.e., the introduced flux jumps times the vertical grid spacing have to exactly match the corresponding cell integrals of the source term. This implies vertical splits of the cell values, and to preserve conservation, the average of left- and right conservative values in a cell have to be identical to its conservative values before the split. In summary, the task consists of splitting the cell values into left and and right values, such that the Rankine-Hugoniot and the conservation conditions are fulfilled. Once completed, clean, homogeneous conditions exist around the vertical cell interfaces, and thus an ordinary Riemann solver (since the source terms

already are accounted for by the split) can be employed to obtain the numerical fluxes. Of course, analogously the fluxes at the horizontal interfaces can be computed. All together, this procedure of computing the numerical fluxes is termed Rankine-Hugoniot-Riemann (RHR) solver.

There is a large body of work regarding hyperbolic systems with source terms, for example [12] and more recently [25] and [26]. The method used here is based on the one described in [21]. Earlier, in [18], this method was devised for general Godunov-type methods, and in [17], a similar idea was proposed, but there the Rankine-Hugoniot jump matching the source term is placed at the interfaces.

As mentioned above, it is important that the cell averages remain unchanged when the Rankine-Hugoniot jump is introduced at the cell centers. Therefore, the conservative values in both cell halves are perturbed by the same amounts δ_x and δ_y (for vertical and horizontal splits, respectively), that is,

$$\begin{aligned} \mathbf{U}_l &= \mathbf{U} - \delta_x & & \mathbf{U}_b = \mathbf{U} - \delta_y \\ \mathbf{U}_r &= \mathbf{U} + \delta_x \quad \text{and} & & \mathbf{U}_t = \mathbf{U} + \delta_y \\ \Rightarrow \mathbf{U} &= \frac{1}{2}\left(\mathbf{U}_l + \mathbf{U}_r\right) & & \Rightarrow \mathbf{U} = \frac{1}{2}\left(\mathbf{U}_b + \mathbf{U}_t\right). \end{aligned} \tag{19}$$

The source term is now divided into the contributions

$$\mathbf{Q}_x = \begin{pmatrix} 0 \\ -m_x/(\rho\lambda k) + g_x\gamma/\lambda \\ 0 \\ 0 \end{pmatrix} \quad \text{and} \quad \mathbf{Q}_y = \begin{pmatrix} 0 \\ 0 \\ -m_y/(\rho\lambda k) + g_y\gamma/\lambda \\ 0 \end{pmatrix} \tag{20}$$

for the x and y-directions, respectively, which are treated separately.

The integrals of the source terms in each direction are approximated as $\Delta x\mathbf{Q}_x$ and $\Delta y\mathbf{Q}_y$, respectively. Across the jumps, the Rankine-Hugoniot jump conditions

$$\mathbf{F}_x(\mathbf{U}_r) - \mathbf{F}_x(\mathbf{U}_l) = \Delta x\mathbf{Q}_x \quad \text{and} \quad \mathbf{F}_y(\mathbf{U}_t) - \mathbf{F}_y(\mathbf{U}_b) = \Delta y\mathbf{Q}_y \tag{21}$$

must hold. From Eqs. (19), (20) and (21) we can derive all values in the cell halves, which are shown in the Appendix A.4.

Since the source term is accounted for by a jump at the cell centers, the piecewise linear reconstruction for the extension to second order is no longer done. Furthermore, neither the source term limiting described in [21] is applied.

Figure 3 shows that the CHSF method with the RHR solver produces much more accu-

rate results of the flow around the nearly impermeable shales, without the second phase penetrating into them. However, one can detect some differences when comparing with the reference solution; this is investigated next.

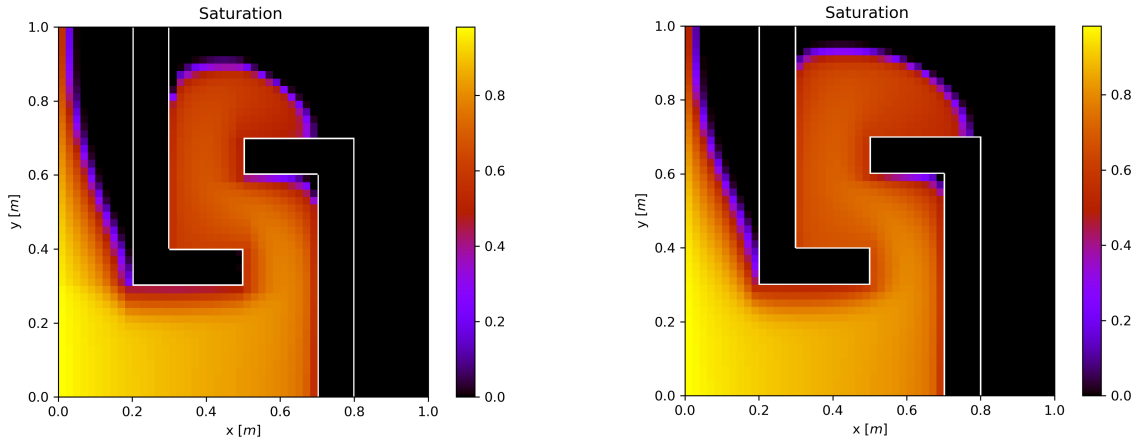


Figure 3: Two phase flow and transport around nearly impermeable shales: The test case is from Figure 2, but compared is the solution obtained with the CHSF method and the RHR solver (left) against the reference obtained with the Implicit Method (right).

Like the ordinary characteristics-based Riemann solver, the Rankine-Hugoniot-Riemann solver is approximate, but crucially it takes into account the source terms, which can be very large in our case. The results of this paper show that it is a better alternative to the ordinary characteristics-based Riemann solver when applied for our hyperbolic system of conservation laws with large source terms.

In the steady state the advantage of the RHR solver over the ordinary characteristics-based Riemann solver is especially evident. This is explained in more detail in Appendix B.1, using the simplified problem from section 2.3.

The ordinary approximate Riemann solver as it was implemented in [16] treats all discontinuities at cell interfaces as shocks. For transsonic rarefaction waves, this can lead to entropy violating solutions [19]. In [16], this was handled by using initial data with sufficiently small jumps. For this paper, the Harten entropy fix [13] was implemented, which is discussed in Appendix B.2.

3.3 Taking 2D Effects into Account

Since the numerical fluxes in the different coordinate directions are treated separately, in this form the RHR solver does not take into account two-dimensional effects, which (as shown later in this section) partly accounts for the discrepancies observed in Figure 3. As shown next, this deficiency can be resolved by exploiting the RHR solver's ability to handle source terms. Rearranging Eq. (10) shows that for each direction we can interpret

the flux gradient in the transverse direction as an additional source term $\mathbf{Q}^+_{x,y}$, that is, one obtains

$$\frac{\partial}{\partial t}\mathbf{U} + \frac{\partial}{\partial x}\mathbf{F}_x(\mathbf{U}) = \mathbf{Q}_x - \underbrace{\frac{\partial}{\partial y}\mathbf{F}_y(\mathbf{U})}_{\mathbf{Q}^+_x} \tag{22}$$

and

$$\frac{\partial}{\partial t}\mathbf{U} + \frac{\partial}{\partial y}\mathbf{F}_y(\mathbf{U}) = \mathbf{Q}_y - \underbrace{\frac{\partial}{\partial x}\mathbf{F}_x(\mathbf{U})}_{\mathbf{Q}^+_y} \tag{23}$$

in horizontal and vertical directions, respectively. Then, the one-dimensional problems at the interfaces are consistent with the full system (10). Taking this additional source term into account is not straightforward, as the flux gradients are not known ahead of the flux calculation. Instead, exponentially weighted time averages of the previously calculated flux gradients are used. The exponential decay of the weights is determined by some parameter ξ, and the additional sources terms are updated as

$$(\mathbf{Q}^+_x)_{n\to n+1} = \xi(\mathbf{Q}^+_x)_{n-1\to n} + (1-\xi)\frac{1}{\Delta y}\left(\mathbf{F}_y^{i,j+1/2} - \mathbf{F}_y^{i,j-1/2}\right)_{n-1\to n}, \tag{24}$$

$$(\mathbf{Q}^+_y)_{n\to n+1} = \xi(\mathbf{Q}^+_y)_{n-1\to n} + (1-\xi)\frac{1}{\Delta x}\left(\mathbf{F}_x^{i+1/2,j} - \mathbf{F}_x^{i-1/2,j}\right)_{n-1\to n}, \tag{25}$$

$$(\mathbf{R}_x)_{n\to n+1} = (\mathbf{Q}_x)_{n\to n+1} - \omega(\mathbf{Q}^+_x)_{n\to n+1} \text{ and} \tag{26}$$

$$(\mathbf{R}_y)_{n\to n+1} = (\mathbf{Q}_y)_{n\to n+1} - \omega(\mathbf{Q}^+_y)_{n\to n+1}. \tag{27}$$

For the cases presented in this paper, we have found that sufficient stability of the scheme could be achieved with the choice $\xi = 0.98$ and with the cross flux gradients only taken into account for the continuity equation and for the normal momentum flux. Thus, at time step n, the systems

$$\frac{\partial}{\partial t}\mathbf{U} + \frac{\partial}{\partial x}\mathbf{F}_x(\mathbf{U}) = \mathbf{Q}_x - \Delta x \begin{pmatrix} (\mathbf{R}_x)^{(1)}_{n-1\to n} \\ (\mathbf{R}_x)^{(2)}_{n-1\to n} \\ 0 \\ 0 \end{pmatrix} \tag{28}$$

and

$$\frac{\partial}{\partial t}\mathbf{U} + \frac{\partial}{\partial y}\mathbf{F}_y(\mathbf{U}) = \mathbf{Q}_y - \Delta y \begin{pmatrix} (\mathbf{R}_y)^{(1)}_{n-1\to n} \\ 0 \\ (\mathbf{R}_y)^{(3)}_{n-1\to n} \\ 0 \end{pmatrix} \tag{29}$$

are considered for the numerical flux calculations at the vertical and horizontal cell interfaces, respectively. The resulting flux solver, based on accounting for the cross flux gradients in the described way and subsequent application of the RHR solver, is termed

multi-dimensional RHR (MD-RHR) solver.

Figure 4 shows that the result obtained with the CHSF method and the MD-RHR (left) compares well to the reference (right).

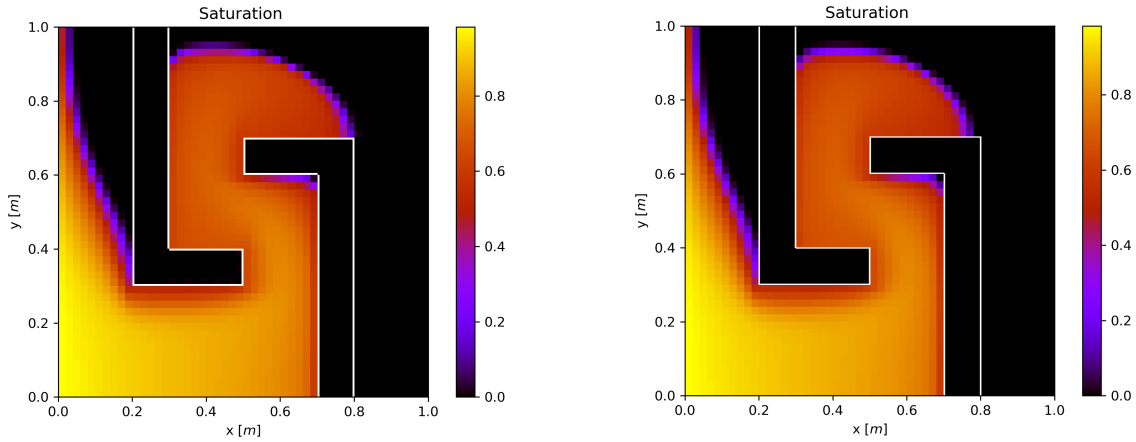


Figure 4: Two phase Flow and transport around nearly impermeable shales: The test case is from Figure 2, but compared is the solution obtained with the CHSF method and the MD-RHR solver (left) against the reference obtained with the Implicit Method (right).

That the CHSF method also works very well for cases with buoyancy is shown in Fig. 5, which depicts results of a case inspired by CO_2 sequestration, where a light plume rises and gets deviated by a nearly impermeable shale with a hole in the middle.

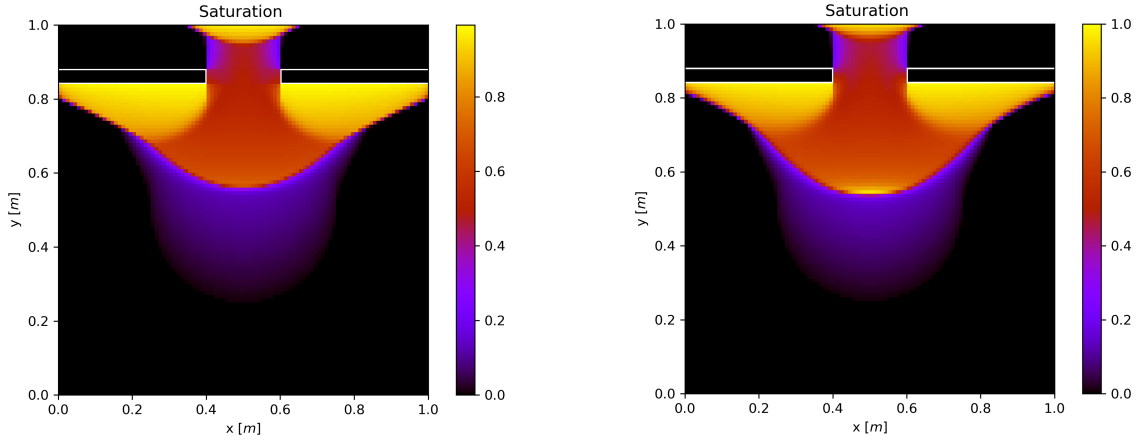


Figure 5: Buoyant two-phase plume with nearly impermeable shale: A plume rises between two nearly impermeable shales (marked by white lines); results obtained with the CHSF method and the MD-RHR solver (left) are compared to the GPRS [1] reference (right).

4 Numerical Experiments

So far, the hyperbolic method has only been tested for very simplified permeability fields. In the following, the hyperbolic method with the MD-RHR solver is tested for the highly heterogeneous, more representative permeability fields taken from model 2 of the SPE10 dataset [7], i.e., the top and the bottom layers are considered for our 2D simulations. In the top layer, the permeability field varies smoothly, while the bottom layer contains distinct, sharp permeability contrasts and coherent meandering channels, which make it a very challenging test case for numerical methods. Two phase flow with constant pressures at the left and right boundaries is considered, and the first phase is injected at the left displacing the second one, which initially occupies the whole domain. As reference, the Implicit Method was used. More information about this test case can be found in Appendix C.2 along with plots of results obtained with different parameters.

4.1 SPE10 Dataset - Top Layer

For the top layer of the SPE10 dataset, as shown in Fig. 6, the CHSF method with the MD-RHR solver can reproduce the reference very accurately; the nontrivial saturation distributions are almost identical.

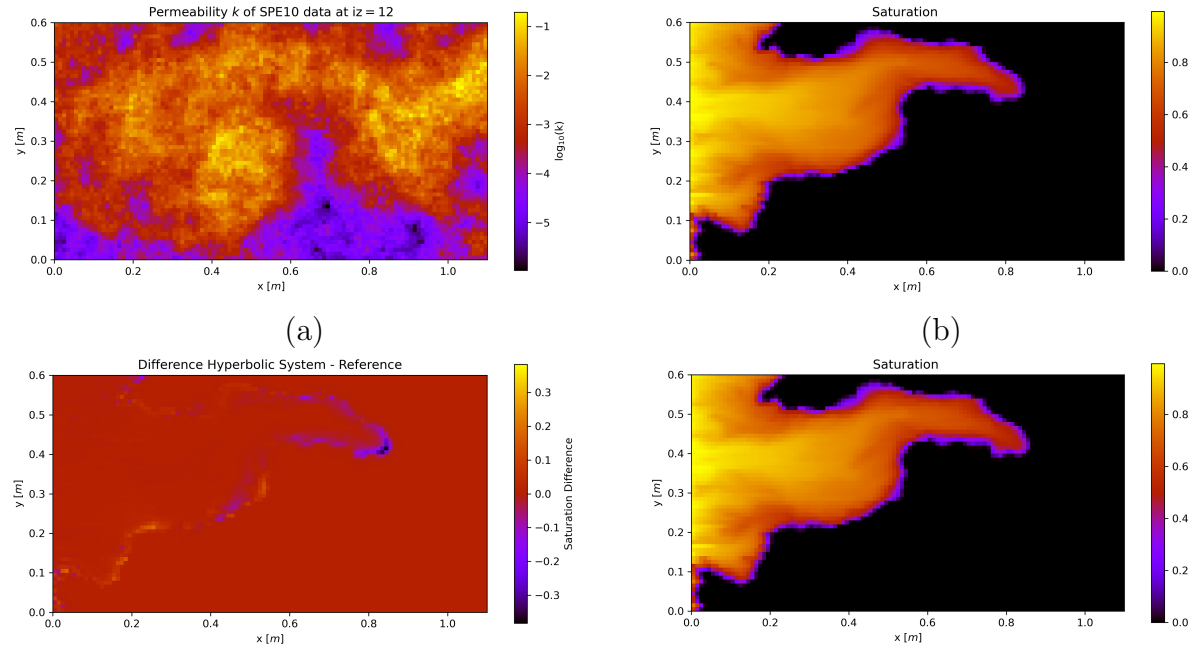


Figure 6: SPE10 top layer with a 100×60 equidistant Cartesian grid. (a): permeability field; (b): saturation map at time $t = 200$ s obtained from the CHSF method with $c = 8$, $\rho_{\text{ref}} = 1$ and the MD-RHR solver; (d): saturation map obtained from a general purpose reservoir simulator; (c) difference between the saturation maps obtained from the two methods.

4.2 SPE10 Dataset - Bottom Layer

Due to the sharp and strong permeability contrasts with the coherent, meandering channels, the bottom layer of the SPE10 dataset is even more challenging for numerical simulations than the bottom layer. As shown in Fig. 7, however, the CHSF solution (Fig. 7b) still compares very well to the reference (Fig. 7d).

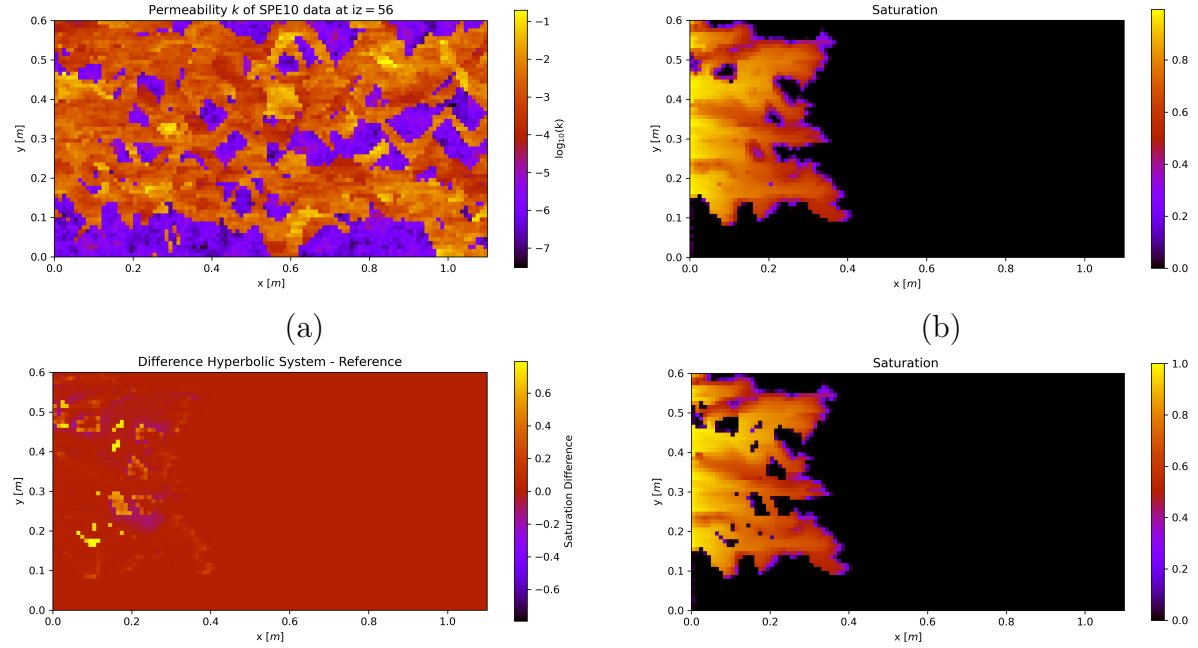


Figure 7: SPE10 bottom layer with a 100×60 equidistant Cartesian grid. (a): permeability field; (b): saturation map at time $t = 200$ s obtained from the CHSF method with $c = 8$, $\rho_{\text{ref}} = 1$ and the MD-RHR solver; (d): saturation map obtained from a general purpose reservoir simulator; (c) difference between the saturation maps obtained from the two methods.

5 Conclusions

In this paper, the coupled hyperbolic subsurface flow (CHSF) method proposed in [16] has been further examined and generalized for heterogeneous permeability fields. It was investigated in depth how performance and accuracy of the CHSF method depend on the choice of parameters. To this end, analytical 1D solutions of the CHSF system were compared to the corresponding analytical solutions of the standard incompressible flow equation. In particular, the choice of parameter c is a trade-off between accuracy and allowed time step size (and thus computational efficiency).

For heterogeneous permeability fields the approximate Riemann solver employed in [16] proved to be too inaccurate. Therefore, a novel multi-dimensional Rankine-Hugoniot-Riemann (MD-RHR) solver was developed, which properly takes into account the source

terms and multi-dimensional effects. It was shown that with this new numerical flux solver the numerical artifacts observed with the previous Riemann solver disappear.

Besides being much more accurate than other Riemenn solvers, the MD-RHR solver is relatively simple to implement and computationally efficient. Note that the ideas which led to the MD-RHR solver presented in this paper are more general and can be applied for other hyperbolic conservation laws.

Several further generalizations of the new CHSF method are envisioned. For example, despite the intrinsically tight coupling between flow and transport, the fact that all operations are local ensures great stability and renders the method ideally suited for massive parallel computation on multiple CPUs and GPUs. Further, conceptually it seems possible to combine the CHSF method with adaptive grid refinement (AGR) [4] and adaptive conservative time stepping (ACTI) [15][22][24]. Implementing all this in 3D and extending the CHSF method's capability to account for more complex physical effects would turn the CHSF method into a very powerful tool.

A Derivations

A.1 Derivation of Fractional Flow Equation

Darcy's law for a single phase can be written as

$$\mathbf{u}_1 = -k\lambda_1 \nabla p - k\lambda_1 \rho_1 \mathbf{g}. \tag{30}$$

First, we rearrange Darcy's law for buoyant two-phase flow for the pressure gradient

$$\nabla p = -\frac{1}{\lambda k}\mathbf{u} + \frac{\gamma}{\lambda}\mathbf{g}. \tag{31}$$

An expression for the Darcy flux of the first phase can be obtained by substituting (31) with the pressure gradient in (30).

$$\begin{aligned} \mathbf{u}_1 &= \frac{\lambda_1}{\lambda}\mathbf{u} - k\frac{\lambda_1}{\lambda}(\lambda_1\rho_1 + \lambda_2\rho_2)\mathbf{g} - k\lambda_1\rho_1\mathbf{g} \\ &= \frac{\lambda_1}{\lambda}\mathbf{u} - k\frac{\lambda_1}{\lambda}(\lambda_1\rho_1 + \lambda_2\rho_2 - (\lambda_1+\lambda_2)\rho_1)\mathbf{g} \\ &= \underbrace{\frac{\lambda_1}{\lambda}}_{f_1}\mathbf{u} + \underbrace{k\frac{\lambda_1\lambda_2}{\lambda}(\rho_1-\rho_2)}_{f_{12}}\mathbf{g}. \end{aligned} \tag{32}$$

A.2 Analytical Solution of Hyperbolic System

We consider a one-dimensional problem with a steady phase flow with a single phase without gravity. As boundary conditions we have a pressure p_{L} on one side of the domain and a velocity u_{R} on the other. The subscripts L and R are used to denote the values at the corresponding ends of the domain.

Darcy's law predicts a divergence free velocity, thus the velocity is constant everywhere. The pressure can be found by integrating Darcy's law as

$$p(x) = p_L + \mu u_R \int_x^{x_L} \frac{1}{k(\hat{x})} d\hat{x}. \tag{33}$$

Next, the solution of the hyperbolic system is derived. As explained in section 2.3, we set

$$p_{\mathrm{L}} = \rho_{\mathrm{ref}} c^2. \tag{34}$$

From the continuity equation we find that the momentum is constant in the domain, i.e.,

$$(\rho u)(x) = m = \text{const.} \tag{35}$$

The momentum balance is given as

$$\frac{\mathrm{d}}{\mathrm{d}x}(\rho u^2 + p) = -\frac{\mu}{k} u. \tag{36}$$

Using $p = c^2 \rho$ and Eq. (35), we arrive at

$$\frac{\mu}{mk} = \left(\frac{c^2}{u^3} - \frac{1}{u} \right) \frac{\mathrm{d}u}{\mathrm{d}x}. \tag{37}$$

Here, μ is a constant and k is a function of x. This ordinary differential equation can be solved using separation of variables. A is the integration constant and is important for enforcing the boundary conditions, leading to

$$\frac{\mu}{m} \int_0^x \frac{1}{k(\hat{x})} \mathrm{d}\hat{x} - A = \int \frac{c^2}{u^3} - \frac{1}{u} \mathrm{d}u = -\frac{1}{2} \frac{c^2}{u^2} + \frac{1}{2} \ln(\frac{1}{u^2}). \tag{38}$$

The goal is to manipulate the right hand side so we can use the Wright omega function ω that solves

$$w + \ln(w) = z \tag{39}$$

for w, with $w, z \in \mathbb{C}$. It is described in detail in [8]. For the next step, complex numbers

have to be introduced. We use n to keep track of the branch of the logarithms.

$$\ln(\frac{1}{u^2}) = \ln(-\frac{c^2}{u^2}) - \ln(-c^2) + 2i\pi n = \ln(-\frac{c^2}{u^2}) - \ln(c^2) + (2n+1)i\pi \tag{40}$$

Using this with Eq. (38) yields

$$-\frac{c^2}{u^2} + \ln(-\frac{c^2}{u^2}) = (2n+1)i\pi + 2\left(\ln(c) + \frac{\mu}{m}\int_0^x \frac{1}{k(\hat{x})}\mathrm{d}\hat{x} - A\right). \tag{41}$$

Using $w = -\frac{c^2}{u^2}$, we can apply Eq. (39) to find u as

$$u^2 = -\frac{c^2}{\omega\left((2n+1)i\pi + 2\left(\ln(c) + \frac{\mu}{m}\int_0^x \frac{1}{k(\hat{x})}\mathrm{d}\hat{x} - A\right)\right)}. \tag{42}$$

We now take a closer look at the argument to ω. One of the terms is the complex number $(2n+1)i\pi$. The real part of the argument is

$$\ln(\frac{c^2}{u_R^2}) - \frac{c^2}{u_R^2} - \underbrace{2\frac{\mu}{m}\int_x^L \frac{1}{k(\hat{x})}\mathrm{d}\hat{x}}_{\geq 0}. \tag{43}$$

Since $c > u_R$,

$$0 < \ln(\frac{c^2}{u_R^2}) \leq \frac{c^2}{u_R^2} - 1, \tag{44}$$

and thus the real part of the argument is less than or equal to -1.

For $n = -1$ and for $n = 0$ the argument lies exactly on the discontinuities of the Wright ω function, called the "doubling lines" in [8]. On these doubling lines, the imaginary part of ω vanishes. However, the real part is not clearly defined there, as one obtains different values when the limit from one side or the other is used. As it turns out, one obtains a valid solution for u in both cases. This reflects the fact that there are two solutions to the equation (37) with the boundary conditions we impose. However, only one of them matches the solution given by Darcy's law. The hyperbolic method will choose the correct solution if the initialization is done correctly, which is usually the case.

The boundary conditions are enforced by finding the appropriate A as

$$A = \frac{\mu}{m}\int_0^L \frac{1}{k(\hat{x})}\mathrm{d}\hat{x} + \frac{1}{2}\frac{c^2}{u_R^2} + \ln(u_R). \tag{45}$$

The momentum m cannot be calculated directly and is determined by iteration. First, m_0 is assumed to be equal to $\rho_{\mathrm{ref}} u_R$ as it should be according to Darcy's law. In each

iteration, m_n is used to find A_n and then

$$u_n(x_L)^2 = -\frac{c^2}{\omega(\ln(-1) + 2\,(\ln(c) - A_n))} \tag{46}$$

$u_n(x_L)$ on the left boundary where the density ρ_{ref} is known. Then $m_{n+1} = \rho_{\text{ref}} u_n(x_L)$ is used for the next iteration.

On the doubling lines, the complex part of the Wright ω function is zero and the real part is negative, so the solution u is real. Furthermore, since we solve for u^2, both a positive and a negative solution for u are found, but only one of them can satisfy the boundary condition. From the momentum m and u, the pressure is easily found by $p = \rho c^2 = mc^2/u$.

A.3 Upper Bound for the Largest Relative Density Difference

The upper bound for the largest relative density difference is derived. We start from equation (36) and consider

$$-\frac{\mathrm{d}\rho}{\mathrm{d}x} = \frac{\mu}{k}\frac{u}{c^2 - u^2}. \tag{47}$$

The mean of the left hand side is found by integration. It is positive and bound by the highest possible value of the right hand side. From Eqs. (33) and (35) we know that $u_{\text{L}} < u_{\text{R}}$ and $\rho_{\text{L}} > \rho_{\text{R}}$ and obtain

$$\frac{1}{L}\int_0^L -\frac{\mathrm{d}\rho}{\mathrm{d}x}\,\mathrm{d}x = \frac{\rho_{\text{L}} - \rho_{\text{R}}}{L} \leq \max\left\{\frac{\mu}{k}\frac{u}{(c^2 - u^2)}\right\} \leq \frac{\mu}{k_{\min}}\frac{u_{\text{R}}}{(c^2 - u_{\text{R}}^2)} \tag{48}$$

$$\frac{\rho_{\text{L}} - \rho_{\text{R}}}{\rho_{\text{L}}} = \delta\hat{\rho}_{\max} \leq \frac{\mu L}{k_{\min}}\frac{u_{\text{R}}}{\rho_{\text{L}}\,(c^2 - u_{\text{R}}^2)} \tag{49}$$

A.4 Calculating the Values in the Cell Halves

Because the continuity equation does not have a source term we obtain that the momentum normal to the jump remains constant across the jump in both x- and y-directions, i.e.,

$$\mathbf{F}_x^{(1)}(\mathbf{U}_r) - \mathbf{F}_x^{(1)}(\mathbf{U}_l) = m_x^r - m_x^l = 0 \;\Rightarrow\; m_x^r = m_x^l = m_x \tag{50}$$

$$\mathbf{F}_y^{(1)}(\mathbf{U}_t) - \mathbf{F}_y^{(1)}(\mathbf{U}_b) = m_y^t - m_y^b = 0 \;\Rightarrow\; m_y^t = m_y^b = m_y. \tag{51}$$

The numbers in the superscript parentheses are indices for the vectors. Next, we find the density ρ in all cell halves using the normal momentum fluxes, i.e.,

$$\mathbf{F}_x^{(2)}(\mathbf{U}_r) - \mathbf{F}_x^{(2)}(\mathbf{U}_l) = (m_x^r)^2/\rho_r + c^2\rho_r - (m_x^l)^2/\rho_l - c^2\rho_l = \Delta x \mathbf{Q}_x^{(2)} \tag{52}$$

$$\mathbf{F}_y^{(3)}(\mathbf{U}_t) - \mathbf{F}_y^{(3)}(\mathbf{U}_b) = (m_y^t)^2/\rho_t + c^2\rho_t - (m_y^b)^2/\rho_b - c^2\rho_b = \Delta y \mathbf{Q}_y^{(3)}. \tag{53}$$

Since m_x^l, m_x^r, m_y^b, and m_y^t are known, we now have to solve a third-order polynomial, This is done with the Newton algorithm, which adds only a small additional cost to the computations compared with the ordinary Riemann solver.

The equations

$$-2(m_x^r)^2\delta_x^\rho + 2c^2(\rho^2 - (\delta_x^\rho)^2)\Delta\rho_x - \Delta x Q^{(2)}(\rho^2 - (\delta_x^\rho)^2) = 0 \tag{54}$$

$$-2(m_y^r)^2\delta_y^\rho + 2c^2(\rho^2 - (\delta_y^\rho)^2)\Delta\rho_y - \Delta y Q^{(3)}(\rho^2 - (\delta_y^\rho)^2) = 0 \tag{55}$$

are solved for the density differences $\delta_x^\rho = \frac{1}{2}(\rho_r - \rho_l)$ and $\delta_y^\rho = \frac{1}{2}(\rho_t - \rho_b)$. The derivatives of the left hand sides are given by the equations

$$-2m_x^2\delta_x^\rho + 2c^2(\rho^2 - (\delta_x^\rho)^2)\delta_x^\rho - \Delta x Q^{(2)}(\rho^2 - (\delta_x^\rho)^2) \tag{56}$$

$$-2m_y^2\delta_y^\rho + 2c^2(\rho^2 - (\delta_y^\rho)^2)\delta_y^\rho - \Delta y Q^{(3)}(\rho^2 - (\delta_y^\rho)^2). \tag{57}$$

These equations can have up to three real solutions, but as long as the densities in the cell halves remain close to the density in the entire cell, the correct solution is usually found by starting the iteration with an initial δ_x^ρ and δ_y^ρ of zero.

Finally, we compute the transverse momentum, i.e.,

$$\begin{aligned} \mathbf{F}_x^{(3)}(\mathbf{U}_r) - \mathbf{F}_x^{(3)}(\mathbf{U}_l) &= m_x^r m_y^r/\rho_r - m_x^l m_y^l/\rho_l = 0 \\ \Rightarrow\ m_y^l &= \rho_l m_y/\rho\ ,\ m_y^r = \rho_r m_y/\rho \end{aligned} \tag{58}$$

$$\begin{aligned} \mathbf{F}_y^{(2)}(\mathbf{U}_t) - \mathbf{F}_y^{(2)}(\mathbf{U}_b) &= m_x^t m_y^t/\rho_t - m_x^b m_y^b/\rho_b = 0 \\ \Rightarrow\ m_x^b &= \rho_b m_x/\rho\ ,\ m_x^t = \rho_t m_x/\rho. \end{aligned} \tag{59}$$

The splitting is not done for the saturation transport equation, as the polynomial equation that would have to be solved does not have a unique solution.

B Concerning the RHR Solver

B.1 Steady-State Problems

In steady state the source term is balanced by the flux gradients as the accumulation term vanishes. Schemes that preserve the solution of a steady-state problem are called "well-balanced" [11]. The ordinary Riemann solver cannot produce the correct solution, because it does not take the source term into consideration for the flux computation but only for the cell update. In contrast, the RHR solver can exactly balance the flux gradients and the source. We show this with an illustrative example.

The RHR solver as described in this paper requires that the permeability is constant in the cells. Thus, we consider the discontinuous piecewise constant permeability function shown in Figure 8.

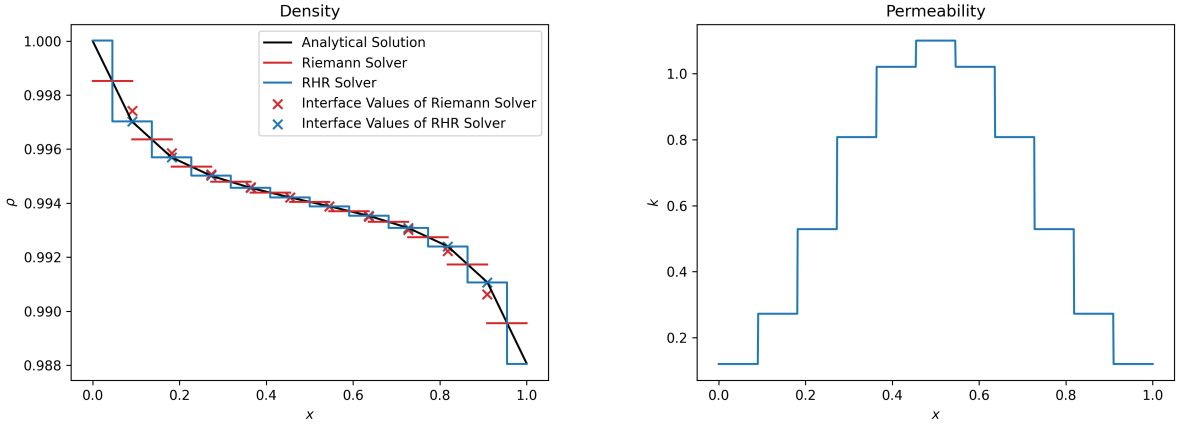


Figure 8: The density obtained analytically, with the ordinary Riemann solver (first order reconstruction), and with the RHR solver for a one-dimensional steady-state pressure-driven problem (left) with a piecewise constant permeability function (right). The crosses show the interface values found by the ordinary Riemann solver (red) and the RHR solver (blue).

We once again use the analytical solution derived in Appendix A.2. If the ordinary Riemann solver is initialized by averaging the analytical solution for each cell, which is the solution the solver should converge to, there are large jumps at the cell interfaces. Because the Riemann solver cannot find the exact fluxes at the interface, it will deviate from the ideal solution.

In contrast, since the source term integrated over the cell is exactly the flux difference across the cell, there are no jumps at the interfaces and the RHR solver will find the exact fluxes. There is no jump at the interfaces and the solution will be exactly maintained.

B.2 Entropy Fix

When transsonic rarefaction waves appear at a cell interface, the Riemann solver sometimes cannot capture this rarefaction, treating it instead as a shock. This leads to solutions that violate the entropy condition. In [16] this was addressed by using initial data that spreads the discontinuity over a few cells. For the Riemann solver with second-order spatial reconstruction this works very well. For the RHR solver we instead decided to implement the Harten entropy fix described in [13]. Figure 9 shows that with the fix, the RHR solver can capture transsonic rarefaction waves.

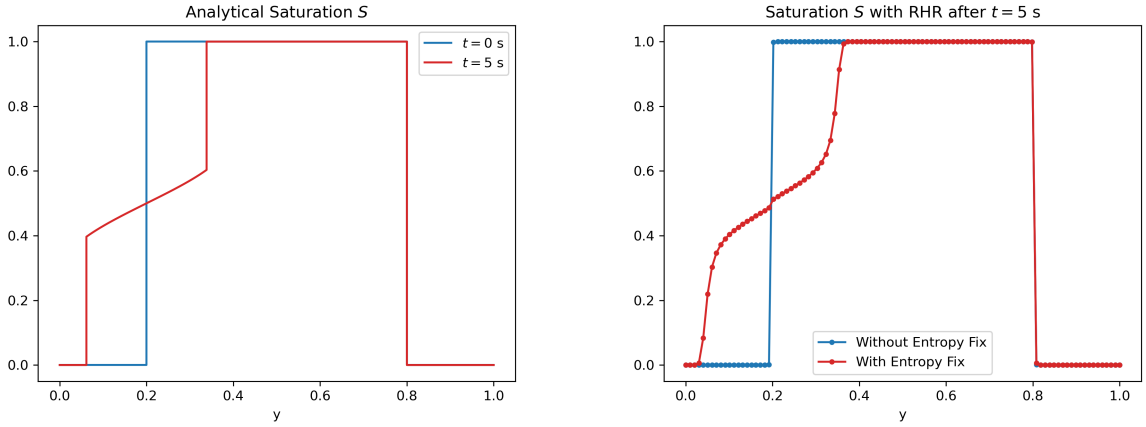


Figure 9: 1D gravity driven problem from [16] with sharp discontinuities. Left: Analytical saturation at $t = 0$ s and $t = 5$ s. Right: Saturation after $t = 5$ s with the RHR solver, both with and without the entropy fix. Sound speed $c = 5$ m/s, reference density $\rho_{\text{ref}} = 1$ kg/m^3, acceleration due to gravity $g = 10$ m/s^2 and density difference between the two phases of $\Delta\rho = 0.1$ kg/m^3.

C Plots

C.1 Plots of $\mathbf{Ma_{max}}$, $\delta\hat{\rho}_{\mathbf{max}}$, and $\mathbf{R_{max}}$

Figures 10 show how the three dimensionless numbers depend on ρ_{ref}, c, and the range of scales of the permeability. The permeability is given by

$$k_\sigma(x) = 10^{\sigma(\sin(2\pi x)^2 - 1)} \tag{60}$$

with σ being the range of orders of magnitudes that the permeability spans.

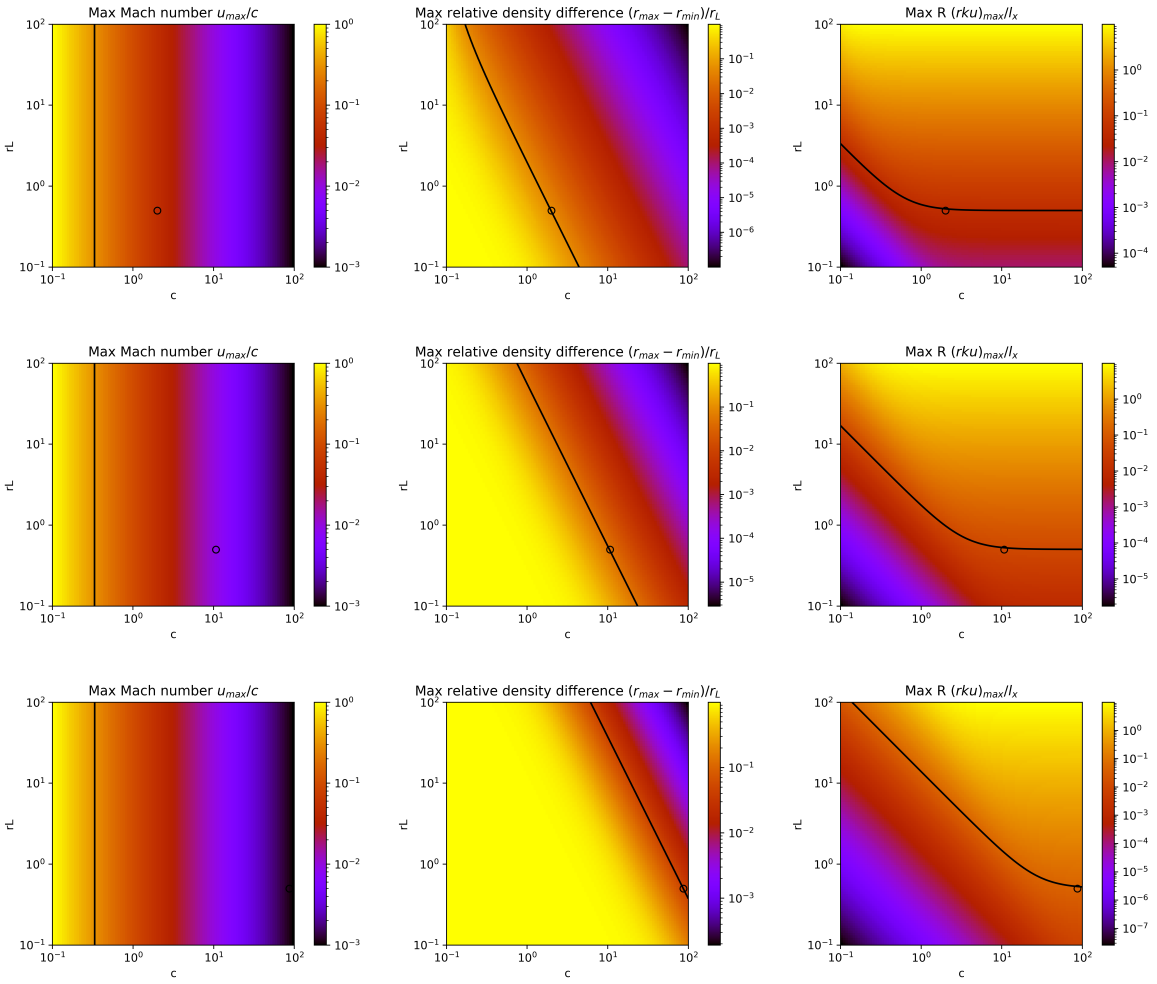


Figure 10: The analytical values of $\mathrm{Ma}_{\max}$, $\delta\hat{\rho}_{\max}$, and $\mathrm{R}_{\max}$ for different combinations of c and ρ_{ref} and different permeability fields. The black lines correspond to a threshold of 0.3, 0.05, and 0.05, respectively. The black circle shows the optimal choice of c and ρ_{ref} that satisfies these thresholds. The permeability is given by equation (60), every row corresponds to a different σ, with $\sigma = 0$, $\sigma = 2$, and $\sigma = 4$, respectively.

C.2 Setup for the SPE10 tests

These tests did not use the full SPE10 dataset. For one, the SPE10 dataset contains a non-isotropic permeability, and the implementation of the hyperbolic method used in this work only works with isotropic permeability (though it would be fairly straightforward to change this). Thus, the permeability value in x-direction from the SPE10 dataset was used as an isotropic permeability value for the cells. The current implementation also only works in two dimensions, so we use slices of the three-dimensional dataset. As the current implementation of the hyperbolic method is not yet fully optimized, it was necessary to only use one half of the slices to reduce computation times.

For the tests, scales that are not typical for geological simulations were used. The length and width of the domain are 1.1 m and 0.6 m, respectively. Both phases have a viscosity of 1 kg/(ms). The pressure difference across the domain is 1 Pa.

The boundary conditions were imposed by setting a pressure in ghost cells on two opposite sides of the domain. The remaining two boundaries have zero-flux boundary conditions. These are not the same boundary conditions as those used for the analytical tests. Setting a pressure difference across the domain is a more realistic setup and it gives better results.

Tables 2 and 3 show the values for $\mathrm{Ma}_{\max}$, $\delta\hat{\rho}_{\max}$, and $\mathrm{R}_{\max}$ as well as the time step size for different combinations of c and ρ_{ref}. The parameters were chosen such that two tests with the same c have similar $\mathrm{Ma}_{\max}$, two tests with the same $p_{\mathrm{ref}} = c^2\rho_{\mathrm{ref}}$ have a similar $\delta\hat{\rho}_{\max}$, and two tests with the same ρ_{ref} have a similar $\mathrm{R}_{\max}$.

	$c = 2, \rho_{\mathrm{ref}} = 1$	$c = 2, \rho_{\mathrm{ref}} = 16$	$c = 8, \rho_{\mathrm{ref}} = 1$	$c = 8, \rho_{\mathrm{ref}} = 16$
$\mathrm{Ma}_{\max}$	0.010169252	0.0082981231	0.0021022299	0.0020740202
$\delta\hat{\rho}_{\max}$	0.24952578	0.015720586	0.015597316	0.0010763012
$\mathrm{R}_{\max}$	0.0023390106	0.035295263	0.002222507	0.035527746
$\Delta t/10^2$ s	0.24818	0.24865	0.06240	0.06242

Table 2: $\mathrm{Ma}_{\max}$, $\delta\hat{\rho}_{\max}$, $\mathrm{R}_{\max}$, and Δt for different combinations of c and ρ_{ref} for the top layer.

	$c = 2, \rho_{\mathrm{ref}} = 1$	$c = 2, \rho_{\mathrm{ref}} = 16$	$c = 8, \rho_{\mathrm{ref}} = 1$	$c = 8, \rho_{\mathrm{ref}} = 16$
$\mathrm{Ma}_{\max}$	0.0065038219	0.0062860783	0.0015724301	0.0015710437
$\delta\hat{\rho}_{\max}$	0.25002178	0.016484454	0.015721561	0.0012794163
$\mathrm{R}_{\max}$	0.0018529918	0.031965425	0.002001431	0.03212357
$\Delta t/10^2$ s	0.24866	0.24901	0.062424	0.062453

Table 3: $\mathrm{Ma}_{\max}$, $\delta\hat{\rho}_{\max}$, $\mathrm{R}_{\max}$, and Δt for different combinations of c and ρ_{ref} for the bottom layer.

C.3 Simulations with different Parameters for the SPE10 Top Layer

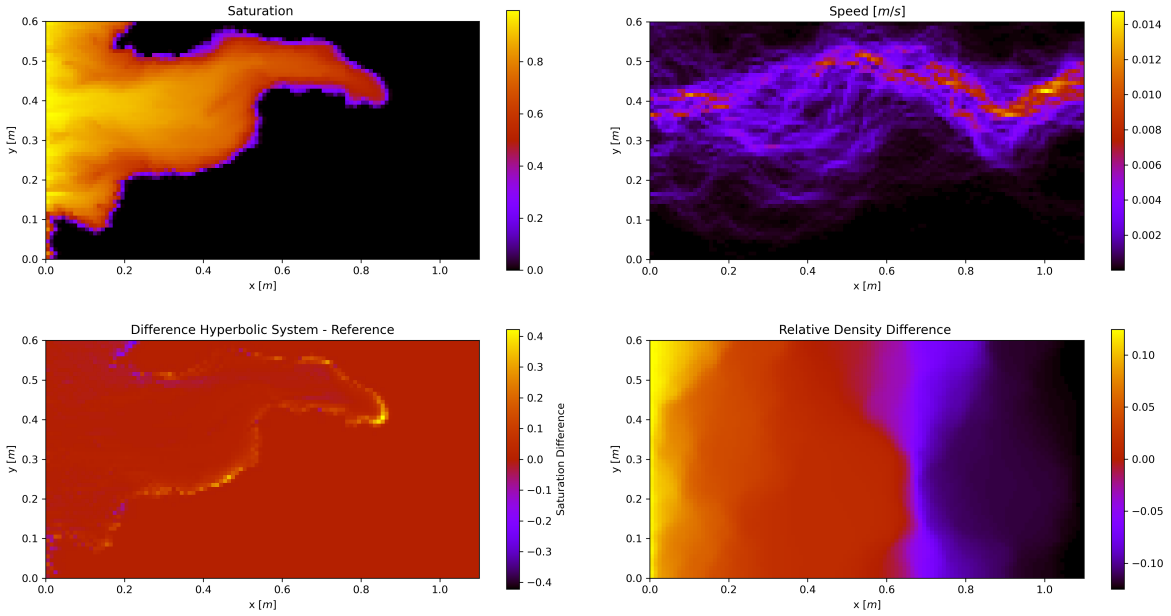


Figure 11: Parameters: $c = 2$ and $\rho_{\text{ref}} = 1$.

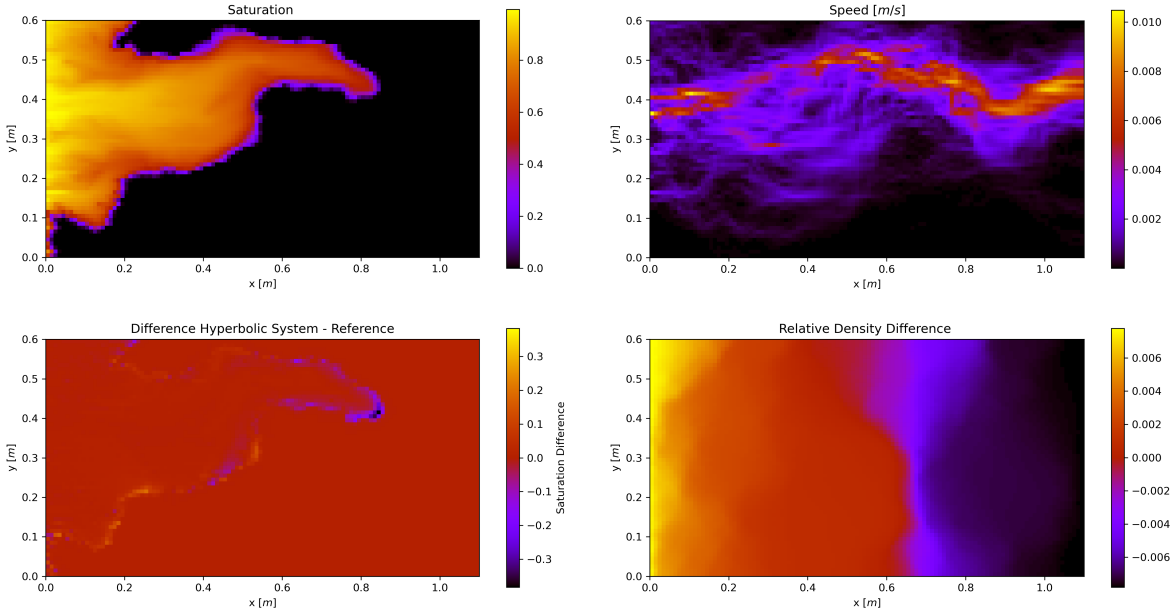


Figure 12: Parameters: $c = 2$ and $\rho_{\text{ref}} = 16$.

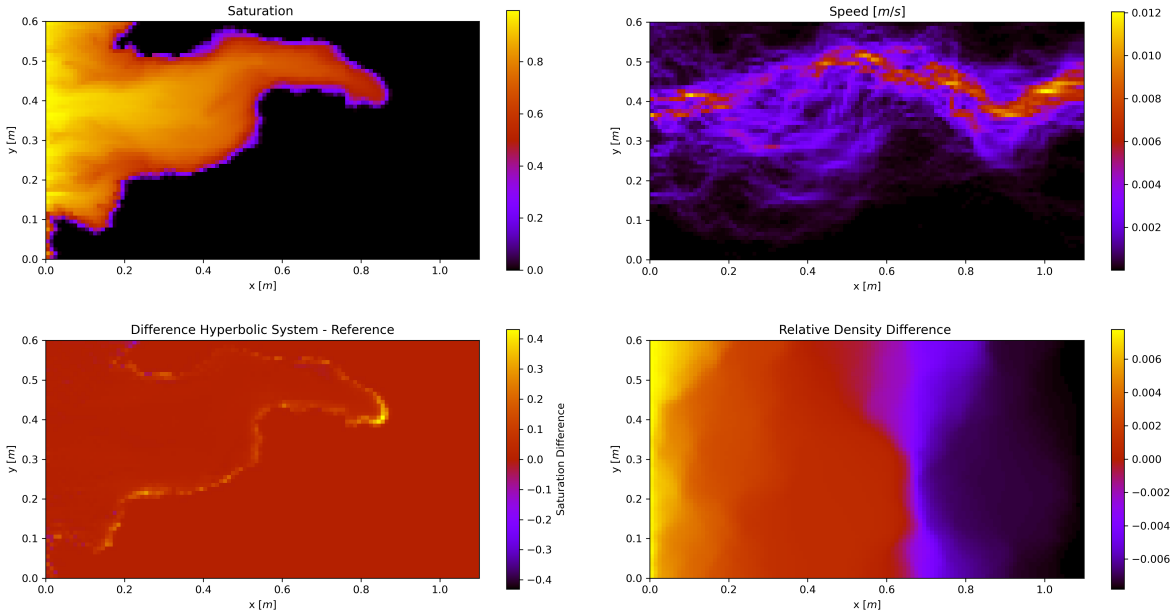


Figure 13: Parameters: $c = 8$ and $\rho_{\text{ref}} = 1$.

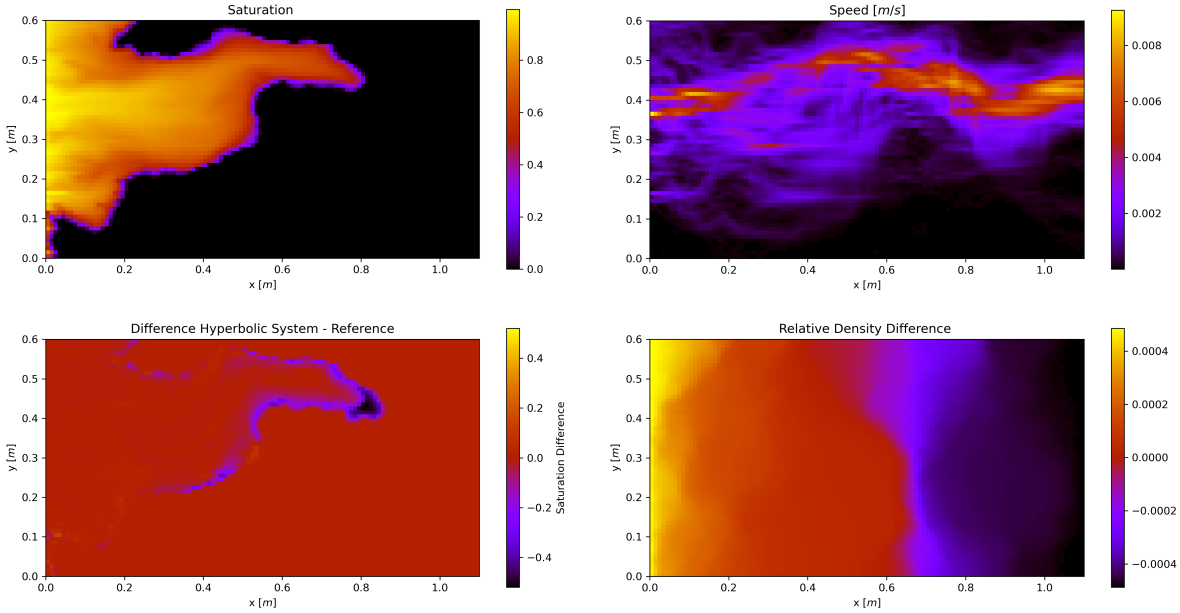


Figure 14: Parameters: $c = 8$ and $\rho_{\text{ref}} = 16$.

C.4 Simulations with different Parameters for the SPE10 Bottom Layer

The bottom layer is a much more challenging permeability. In a few cells, the method cannot compute the saturation correctly, resulting in negative values, which is unphysical. For the saturation plots, the values were clipped at 0 and 1.

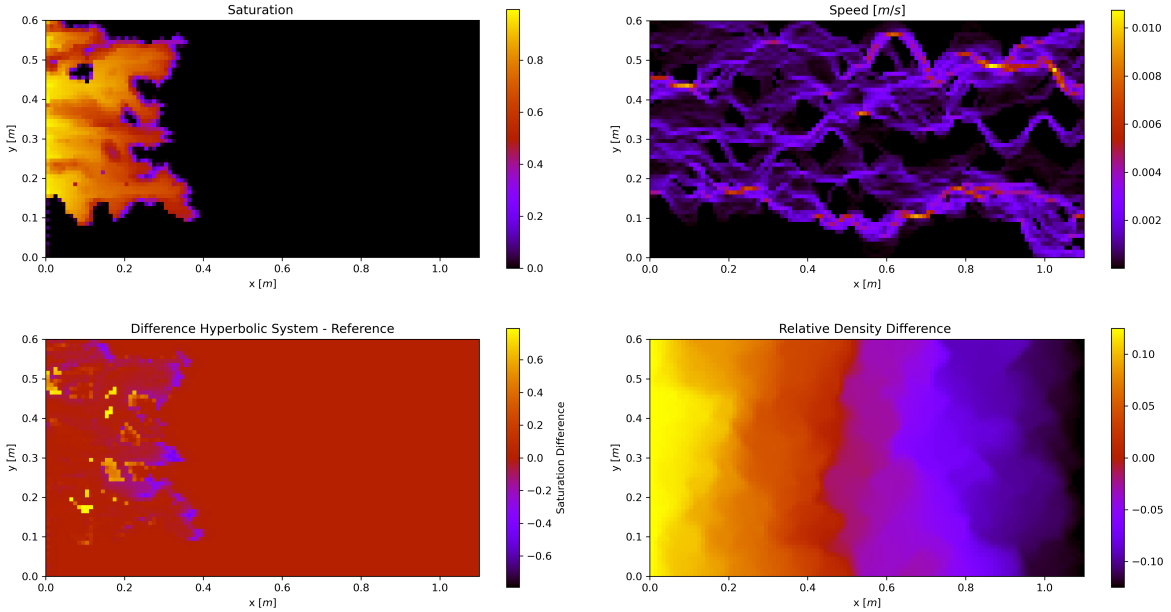


Figure 15: Parameters: $c = 2$ and $\rho_{\text{ref}} = 1$.

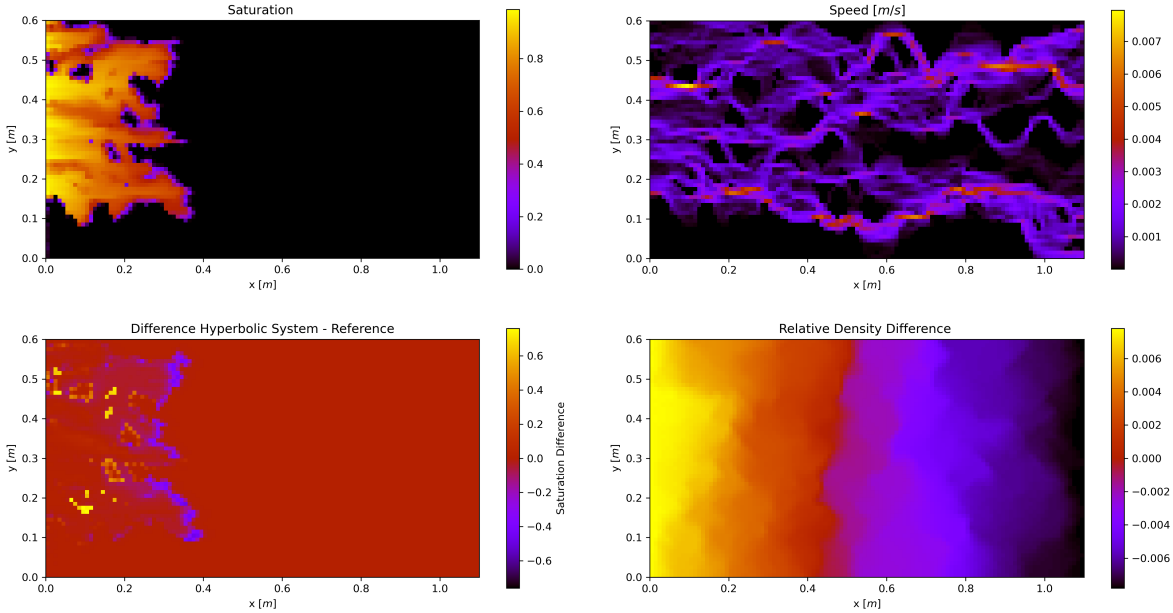


Figure 16: Parameters: $c = 2$ and $\rho_{\text{ref}} = 16$.

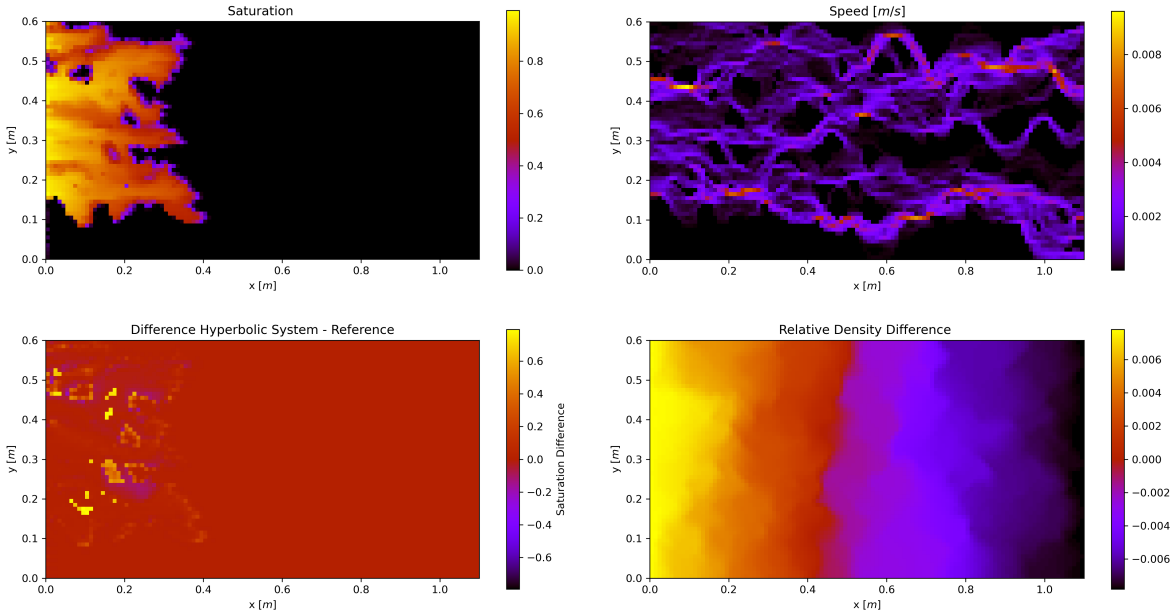


Figure 17: Parameters: $c = 8$ and $\rho_{\text{ref}} = 1$.

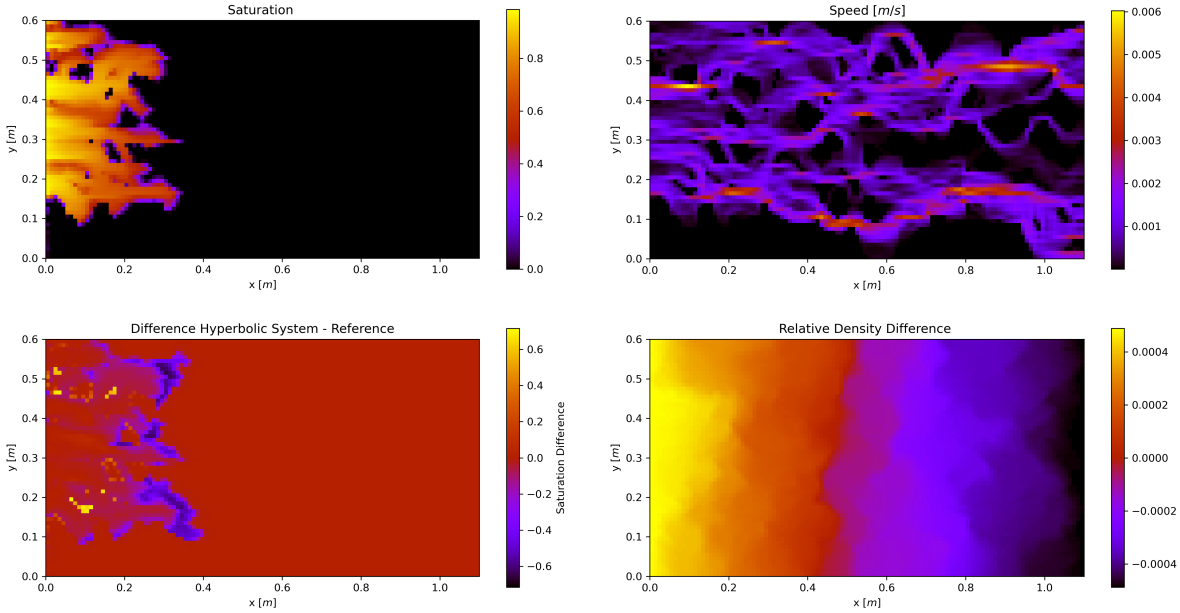


Figure 18: Parameters: $c = 8$ and $\rho_{\text{ref}} = 16$.

References

[1] AD-GPRS. (2025). Automatic Differentiation General Purpose Research Simulator (AD-GPRS) [Stanford University].

[2] Anderson, J. (2016). *Fundamentals of aerodynamics*. McGraw-Hill Education. https://books.google.ch/books?id=D1ZojgEACAAJ

[3] Aziz, K., & Settari, A. (1979). *Petroleum reservoir simulation*. Elsevier Applied Science Publishers, London, UK.

[4] Berger, M. J., & Oliger, J. (1984). Adaptive mesh refinement for hyperbolic partial differential equations. *Journal of Computational Physics*, *53*(3), 484–512. https://doi.org/10.1016/0021-9991(84)90073-1

[5] Buckley, S., & Leverett, M. (1942). Mechanism of Fluid Displacement in Sands. *Transactions of the AIME*, *146*(01), 107–116. https://doi.org/10.2118/942107-G

[6] Chiodaroli, E., De Lellis, C., & Kreml, O. (2014). Global ill-posedness of the isentropic system of gas dynamics. *Communications on Pure and Applied Mathematics*, *68*(7), 1157–1190. https://doi.org/10.1002/cpa.21537

[7] Christie, M. A., & Blunt, M. J. (2001). Tenth SPE Comparative Solution Project: A Comparison of Upscaling Techniques. *SPE Reservoir Evaluation & Engineering*, *4*(4), 308–317. https://doi.org/10.2118/72469-PA

[8] Corless, R. M., & Jeffrey, D. J. (2002). The wright ω function. *Artificial Intelligence, Automated Reasoning, and Symbolic Computation*, 76–89.

[9] Erfani, H., Babaei, M., & Niasar, V. (2021). Dynamics of co2 density-driven flow in carbonate aquifers: Effects of dispersion and geochemistry. *Water Resources Research*, *57*(4). https://doi.org/10.1029/2020WR027829

[10] Goda, H. M., & Behrenbruch, P. (2004, October). *Using a modified brooks-corey model to study oil-water relative permeability for diverse pore structures* (Vol. SPE Asia Pacific Oil and Gas Conference and Exhibition). https://doi.org/10.2118/88538-MS

[11] Godlewski, E., & Raviart, P.-A. (2021). *Numerical approximation of hyperbolic systems of conservation laws*. Springer New York, NY.

[12] Greenberg, J. M., & Leroux, A. Y. (1996). A well-balanced scheme for the numerical processing of source terms in hyperbolic equations. *SIAM Journal on Numerical Analysis*, *33*(1), 1–16. https://doi.org/10.1137/0733001

[13] Harten, A. (1997). High resolution schemes for hyperbolic conservation laws. *Journal of Computational Physics*, *135*(2), 260–278. https://doi.org/https://doi.org/10.1006/jcph.1997.5713

[14] Heinemann, N., Alcalde, J., Miocic, J. M., Hangx, S. J. T., Kallmeyer, J., & al. (2021). Enabling large-scale hydrogen storage in porous media – the scientific challenges. *Energy Environ. Sci.*, *14*, 853–864. https://doi.org/10.1039/D0EE03536J

[15] Jenny, P. (2020). Time Adaptive Conservative Finite Volume Method. *Journal of Computational Physics*, *403*, 109067. https://doi.org/10.1016/j.jcp.2019.109067

[16] Jenny, P., Hasanzade, R., & Tchelepi, H. (2023). Tightly coupled hyperbolic treatment of buoyant two-phase flow and transport in porous media. *Journal of Computational Physics*, *489*, 112–205. https://doi.org/10.1016/j.jcp.2023.112205

[17] Jenny, P., & Müller, B. (1998). Rankine–hugoniot–riemann solver considering source terms and multidimensional effects. *Journal of Computational Physics*, *145*(2), 575–610. https://doi.org/10.1006/jcph.1998.6037

[18] LeVeque, R. J. (1998). Balancing source terms and flux gradients in high-resolution godunov methods: The quasi-steady wave-propagation algorithm. *Journal of Computational Physics*, *146*(1), 346–365. https://doi.org/10.1006/jcph.1998.6058

[19] LeVeque, R. J. (2002). *Finite volume methods for hyperbolic problems*. Cambridge University Press.

[20] Lie, K.-A. (2019). *An introduction to reservoir simulation using matlab/gnu octave: User guide for the matlab reservoir simulation toolbox (mrst)*. Cambridge University Press.

[21] Lund, H., Müller, F., Müller, B., & Jenny, P. (2014). Rankine–hugoniot–riemann solver for steady multidimensional conservation laws with source terms. *Computers & Fluids*, *101*, 1–14. https://doi.org/10.1016/j.compfluid.2014.05.022

[22] Luther, J., Wang, Y., & Jenny, P. (2024). Adaptive conservative time integration for unsteady compressible flow. *Journal of Computational Physics*, *517*, 113324. https://doi.org/10.1016/j.jcp.2024.113324

[23] Mishra, S. (2018). On the convergence of numerical schemes for hyperbolic systems of conservation laws. *Proceedings of the International Congress of Mathematicians (ICM 2018)*, 3641–3668. https://doi.org/10.1142/9789813272880_0195

[24] Wang, Y., Luther, J., Jenny, D., & Jenny, P. (2026). Dynamic space-time adaptive volume-of-fluid method for compressible two-phase flows. *Computer Methods in Applied Mechanics and Engineering*, *449*, 118514. https://doi.org/10.1016/j.cma.2025.118514

[25] Yu, C., Liu, T. G., & Feng, C. (2023). A well-balanced scheme for euler equations with singular sources. *SIAM Journal on Scientific Computing*, *45*(4), A2119–A2151. https://doi.org/10.1137/22M1473224

[26] Zhang, Q., Wan, Y., & Yu, C. (2023). Singular solutions to the riemann problem for the pressureless euler equations with discontinuous source term. *Applicable Analysis*, *102*(14), 3822–3841. https://doi.org/10.1080/00036811.2022.2098729